Isabel Guillamón, Jose Gabriel Rodrigo, Sebastián Vieira, and Hermann Suderow

1 Imaging vortices in superconductors: from the atomic scale to macroscopic distances

Abstract: The Scanning Tunneling Microscope (STM) was used at cryogenic temperatures soon after its invention in the early 1980s. However, it has only been a few years since its full potential for studying superconductors has been developed. Here we provide an introduction to cryogenic STM applied to superconductors and the superconducting vortex lattice. We review STM basics, explaining how we measure the superconducting density of states by atomic-scale tunneling. We also discuss Andreev and Josephson features in tunneling conductance and the direct visualization of thermally induced vortex depinning, vortex motion and vortex melting. Finally, we discuss how to analyze large-scale vortex images, explaining calculations of angular and positional correlation functions and the displacement correlator, and show how these characterize the degree of disorder in the vortex lattice.

Keywords: Scanning probe microscopy, Tunneling spectroscopy, vortex physics, superconductivity.

1.1 Introduction

Tunneling spectroscopy is useful to the study of superconductors because it directly provides the superconducting density of states. In junctions formed by two superconductors, Tunneling spectroscopy also shows the coupling of the Cooper pair wavefunctions through the Josephson effect. During the 1960s and 1970s, many Tunneling spectroscopy experiments were performed. These used layers of an insulating material to form a tunnel barrier for electron transport between the two electrodes. The experiments were often quite conclusive, providing strong experimental support for the Bardeen Cooper and Schrieffer (BCS) theory through the measurement of the superconducting gap and of the electron-phonon pairing interaction in many different materials (see for example [1]).

The invention of the Scanning Tunneling Microscope (STM) by [2] opened the door to tunneling experiments at atomic level, having vacuum as the tunnel barrier. The superconducting tunneling conductance was first measured using an STM by [3] in the technologically important material Nb_3Sn. Subsequent tunneling conductance mea-

Isabel Guillamón, Jose Gabriel Rodrigo, Sebastián Vieira, Hermann Suderow, Laboratorio de Bajas Temperaturas y Altos Campos Magnéticos, Unidad Asociada UAM/CSIC, Departamento de Física de la Materia Condensada, Instituto de Ciencia de Materiales Nicolás Cabrera and Condensed Matter Physics Center (IFIMAC), Universidad Autónoma de Madrid, Spain

DOI 10.1515/9783110456806-002,

surements using STM were done in the cuprates by [4] and [5]. With an STM, one can also perform scanning tunneling spectroscopy and obtain maps of the tunneling conductance as a function of the position with atomic resolution. This makes the STM at low temperatures the only instrument able to map the superconducting density of states with a spatial resolution far below the superconducting coherence length ξ. The Abrikosov vortex lattice was first observed using an STM by [6], with a spatial resolution that exceeded considerably all other vortex visualization techniques.

The key constructive element of the STM is the piezoelectric ceramic, which literally plays the role of a finger touching the nanoworld. In fact, when the STM was invented, people immediately realized the potential of the idea behind it, developing a whole set of new methods to probe matter at the nanoscale by tracing other probes as a function of the position, as for example the force between a tip and the sample. Very soon after the invention of the STM, [7] developed the atomic force microscope, which is today widely used in physics, chemistry and biology. Different probes measuring magnetic fields at the surface were also developed, in particular with more recent advances in nanometric fabrication. Detailed images of vortex lattices have been obtained using magnetic force microscopy, scanning SQUID microscopy, and scanning Hall microscopy. These efforts are reviewed in [8, 9] and [10].

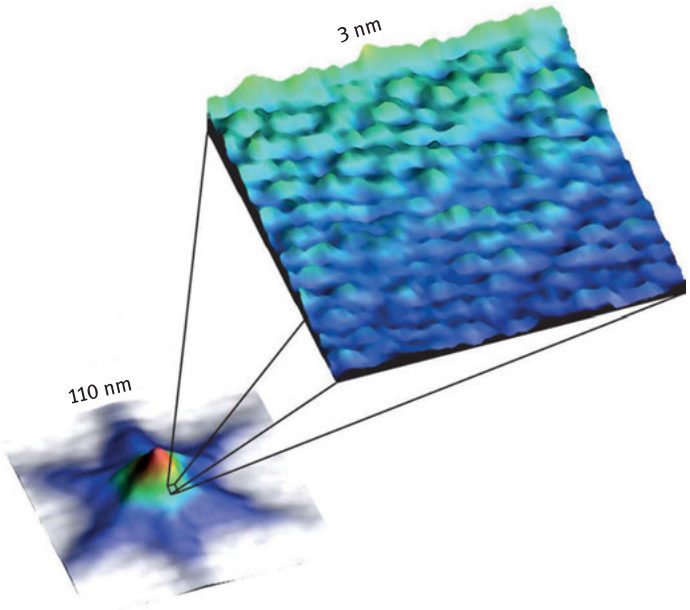

Fig. 1.1: Superconducting vortex in 2H-$NbSe_2$ imaged using STM at length scales of the order of several hundred nm (bottom) and at atomic scale (top). The figures show maps of the zero bias conductance acquired at 0.1 K and 0.03 T. There is a strong spatial variation of the superconducting density of states at all length scales, including at atomic distances. Figure adapted from Ref.[11].

As so often, opening a new window into smaller length scales provides information that could not have been anticipated previously. For example, the features in the superconducting density of states at length scales well below the superconducting coherence length ξ shown in Figure 1.1. This does not conform with the conventional view of superconductivity being homogeneous below ξ.

In this tutorial we explain the main concepts needed to design and understand this and other STM experiments in superconductors. We start by introducing the differences between macroscopic and atomic size tunneling and the role of the distance between tip and sample in normal and superconducting phases. We then discuss the results obtained from maps of the superconducting properties as a function of the position at different length scales, ranging from subnanometer to micrometer scales.

We focus mostly on work performed by our group. We also mention work by other groups whenever needed to explain concepts. But we do not aim at providing a complete reference list. For this, we refer to the reviews by [12, 13] and [14].

1.1.1 Formalisms to treat atomic size tunneling

One of the reasons for the success of STM is that the requirements to obtain atomic resolution on a surface are not as stringent as one may think a priori. One needs of course an atomically flat surface. But the tip can be totally blunt at nm length scales, mostly because the tunneling current depends exponentially as a function of the distance between both tunneling elements. Thus, the tunneling current decreases exponentially and only the outermost tip's atom provides a sizeable tunneling current.

Furthermore, the vacuum tunneling problem can be understood in simple terms for most purposes. Tunneling experiments are based on the quantum mechanical overlap between tip and sample's electronic wavefunctions, which is in general nearly impossible to calculate accurately. The nature of the tip's atom involved in tunneling is not known, it may be an atom of the tip's material (often Pt or Au) but it might well also be an atom picked up from the surface during the scanning process. Even less is known about what kind of electronic orbitals couple together. It turns out that, for most practical processes, the details of the quantum mechanical overlap between tip and sample's electronic wavefunctions do not matter. [15] found that the resulting tunneling current at zero bias voltage and zero temperature is simply proportional to the Fermi level local density of states of the sample at the position of the tip. They used a perturbative treatment of the tunneling current, valid when the overlap between wavefunctions is small, or, for practical purposes, when the tip is sufficiently far apart. Their treatment is based on Bardeen's transfer Hamiltonian formalism and requires knowing the shape of the tip and sample wavefunctions. [16] and [17] assume an s-wave tip wavefunction and find that the STM experiment provides a spatial map of the electronic density of states at an energy fixed by the bias voltage. The current

versus bias voltage can be written as

$$I(V) \propto \int N_S(E) N_T(E - eV) \left(f(E) - f(E - eV)\right) \mathrm{d}E \tag{1.1}$$

where $N_S(E)$ is the sample's density of states, $N_T(E)$ is the tip's density of states and $f(E)$ the Fermi function. The derivative of $I(V)$ is the convolution of $N_T(E)N_S(E)$ with the derivative of the Fermi function. The tunneling matrix elements are part of the proportionality factor. Their energy and spatial dependence are often neglected, although generally this is not true. The energy scale for the superconducting gap is typically far below the energy scales of localized states within the junction and of the energy range where the density of states of the tip $N_T(E)$ varies. Therefore, for most purposes, the tunneling conductance maps $N_S(E)$ of superconductors with enough accuracy at atomic scale.

1.1.2 Electronic scattering and Fermi wavelength

Most superconductors are good metals. Tunneling into an atomically flat metal can also be understood as tunneling into a Fermi sea of free electrons, or a Fermi liquid in the presence of interactions. Actually, this is a classical problem of STM. In practically all discussions about STM imaging, there is a dichotomy between tunneling into localized atomic orbitals and tunneling into the Fermi sea of free (or interacting) electrons. Both points of view lead to radically different images (Figure 1.2a,b and c). Tunneling into atomic orbitals provides the atomic positions at the surface. Tunneling into the Fermi sea, by contrast, provides flat images often with no atomic resolution. In exchange, disturbances to the Fermi sea in the form of defects, step edges or impurities appear as wave-like patterns, whose periodicity is given by the Fermi wavelength λ_F. The STM can be used to trace these patterns as a function of the energy and to measure the dispersion relation for occupied and empty electronic states.

An isolated charge in a free electron system is screened away by changes in the local electron density. This is described in the simplest way within the Thomas–Fermi approximation. Taking into account Bloch wavefunctions leads to Friedel oscillations, which quite often provide the actual answer of a free electron system to an impurity (see for example the book of [18]). Ideally, scanning over a free electron gas with a metallic tip provides flat and featureless images, because the electronic density of the sample is independent of the position. Close to a scattering center, such as an impurity or a step edge, Friedel oscillations produce variations in the local electronic density at the surface. These oscillations are detected in an STM and their energy dependence provides the corresponding dispersion relation. Surfaces of simple metals such as Au or Ag have been extensively studied for example by [19], [20] and [21]. Defects having a preferred orientation, such as step edges or structured impurities (e.g., dimers or chains), provide patterns with higher densities of states along certain directions. The

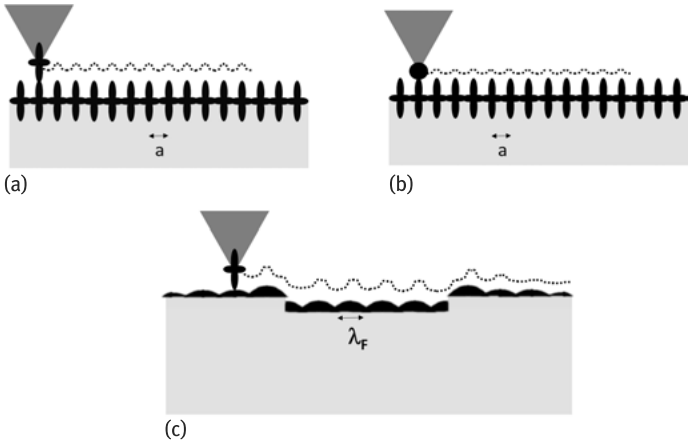

Fig. 1.2: In (a) and (b) we show a schematic view of different tip wavefunctions, eventually leading to different corrugations in the STM images. The sample is represented by the light gray rectangle and the outgoing atomic wavefunctions by the dark orbital-like features. The tip is represented by the dark gray triangle. The wavefunction of the atom at the tip apex is shown in black. The dashed line gives the signal sent to the feedback loop that maintains a constant current between tip and sample. The corresponding periodicity provides the atomic lattice. In (c) we schematically discuss the situation found in metals with strongly delocalized electron wavefunctions. The bulk electron wavefunctions are scattered at the surface at step edges, leading to oscillations in the density of states (dark structures on top of the sample's surface) with a wavelength of λ_F. Scanning the tip over the surface then provides periodic structures with wavelength λ_F.

energy dependence then gives the electronic dispersion relation along these directions only. If impurities or defects are point-like, the conductance images provide directly the reciprocal state shape of the electronic dispersion relation (see for example [22]).

In Figure 1.3a we present cartoon pictures of possible patterns observed at the surface. On the top left panel of Figure 1.3a we show a circular pattern created by a point-like impurity in a system with a circular Fermi surface. In the top right panel we show the pattern formed by a step edge located in the middle of the panel ($x = 0$) in a system with a spherical Fermi surface. In the bottom left panel we show patterns by two perpendicular step edges. In the bottom right panel we show the pattern obtained by a point-like impurity in a system with a square Fermi surface with sides along the x- and y-axis of the figure. In Figure 1.3b we represent the dispersion relation of a hole band. The energy dependence of the surface patterns for the case of a spherical Fermi surface are shown in the bottom panels in reciprocal space. There are circular features with higher intensity at the wavevectors given by the dispersion relation at $E = eV$, where e is the electron charge and V the applied bias voltage. The size of the k-space feature decreases with increasing energy in a hole band, and the opposite can be expected for an electron band.

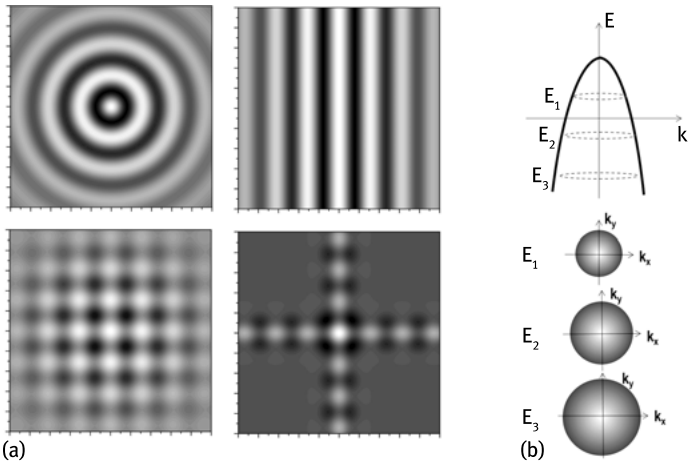

Fig. 1.3: In (a) we represent schematically the expected local density of states in real space at the surface of metals with a defect or impurity in 2D color maps. The value of the density of states is given by the color scale (white being the highest). We show four different cases in (a), a point-like impurity (upper left panel), a linear defect (upper right panel), two perpendicular linear defects (lower left panel) and a strongly anisotropic, square fold, Fermi surface (lower right panel). In (b) we represent (thicker line) schematically a dispersion relation in the top panel and the reciprocal space patterns expected for varying energies in the bottom panels.

The intensity of the observed modulations is given by the imaginary part of the Green function, which in turn includes the bare electron dispersion relation modified by correlations. Kinks in the band structure, van Hove singularities or places with strong electron-phonon scattering provide modified intensities at the relevant energies. This can be dramatic in some systems, such as the cuprate superconductors, where most of the scattering comes from a set of wavevectors connecting parts of the Fermi surface with an enhanced electronic density of states (see for example [23] or [12]), or in the pnictide superconductors, where the nematic electronic properties provide preferred scattering along certain directions (see for a review [13]). Conversely, knowing in advance the band structure and character of the impurity can be useful to locate an impurity embedded in the material, as shown by [24].

1.1.3 Tunneling with multiple conductance channels

A magnetic impurity embedded in a metal often produces a Kondo effect at low temperatures. The Kondo mechanism quenches the spin of the impurity by producing a singlet state with an electronic cloud surrounding the impurity (see for example the book of [18]). Therefore, tunneling into a Kondo impurity occurs in two channels in parallel, one into the free electron cloud and another one into the localized magnetic state of the impurity. The two tunneling conductance channels interfere. The result is

a tunneling density of states that can be described by a Fano lineshape (see [25]). The density of states is a dip in the case of dominant tunneling into the bound state, or a peak in the case of dominant tunneling into the free electron cloud, as schematically shown in Figure 1.4. The Fano anomaly occurs around single magnetic impurities. It has been studied by [26] and more recently in experiments with isolated molecules on metal surfaces by [27]. The Fano anomaly has been also observed in electronic systems having multiple bands crossing the Fermi level with very different effective masses, such as heavy fermions (see for example [28–30] or [31]).

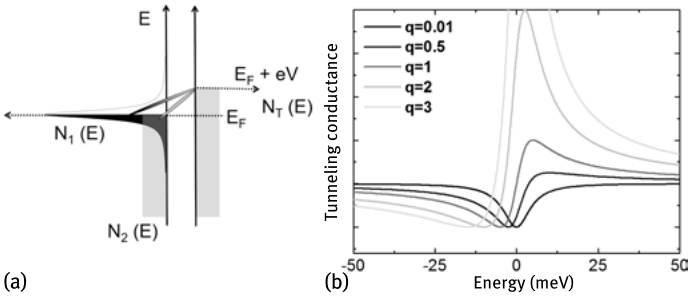

Fig. 1.4: In (a) we show a cartoon picture of the density of states of a band structure consisting of heavy (black) and light (light gray) bands in the sample (left side of the junction). Tunneling occurs from the tip (right side of the junction) which has a simple one band density of states. Eventually, tunneling can occur into each of the bands separately, in which case, there will be interference between tunneling into localized states and into the continuum. The result is a Fano anomaly, shown in (b). For this scheme, we use an energy width of the localized states of $\Gamma = 5$ meV and $E_0 = 0$ meV. The relative strength of tunneling into the resonant state is given by q. For large q, tunneling is into the resonant state, providing a near-Lorentzian shaped tunneling conductance. For low q, the phase shift due to tunneling into the resonant state produces destructive interference and a dip.

1.1.4 From tunneling into contact: Normal phase

When a normal metal tip is moved from tunneling distance to the sample, the wavefunctions overlap. Upon increasing the connection among both electrodes, there comes a point where the wavelike nature of transport is totally lost. Then, the conductance is given by Sharvin's formula which provides the tunneling conductance when transport is in the ballistic regime. Transport is classical, but the contact radius a is far below the electronic mean free path. In between, there is an interesting regime, where the conductance occurs just through a single atom. [32] showed that the chemical nature of the contacting atom determines the precise value of the conductance, which is a multiple of the quantum of conductance $\sigma_0 = \frac{2e^2}{h}$, with e being the electron charge and h Planck's constant (see for example [33] or [34]).

1.1.5 From tunneling into contact: Superconducting phase

Let us consider the situation where two electrodes made of the same superconducting material are slowly moved into contact at zero temperature. When both electrodes are separated in the tunneling regime, single quasiparticle tunneling is possible only for applied voltages larger than two times the superconducting gap of the electrodes (i.e., $eV > 2\Delta$, see Figure 1.5a). For voltages below 2Δ, Andreev reflection provides a conduction mechanism. It involves multiple crossings of the tunneling barrier, as we discuss below. Thus, the Andreev current is further exponentially suppressed with respect to the usual quasiparticle tunneling. The Andreev current is found using Bogoliubov equations, which are the equivalent of the Schrödinger equation for electrons in normal metals for superconductors (see for example the book by [35]).

In an S-S junction, the Andreev conduction mechanism implies multiple reflections through the junction. For $eV < 2\Delta$, electron-like excitations of electrode 1 cannot enter into the gap region of electrode 2 as a single quasiparticle. However, we can find a hole-like quasiparticle with opposite wavevector and spin in the same electrode. This produces a Cooper pair in electrode 2 and a current with $2e$ flows through the junction (Figure 1.5b). The hole-like quasiparticle is reflected into electrode 1 within the region of occupied electron-like states of electrode 1. This was first discussed by Blonder, Tinkham and Klapwijk (BTK) in experiments in macroscopic N-S junctions ([36]). The appendix of that paper shows the procedure needed to obtain the current-voltage

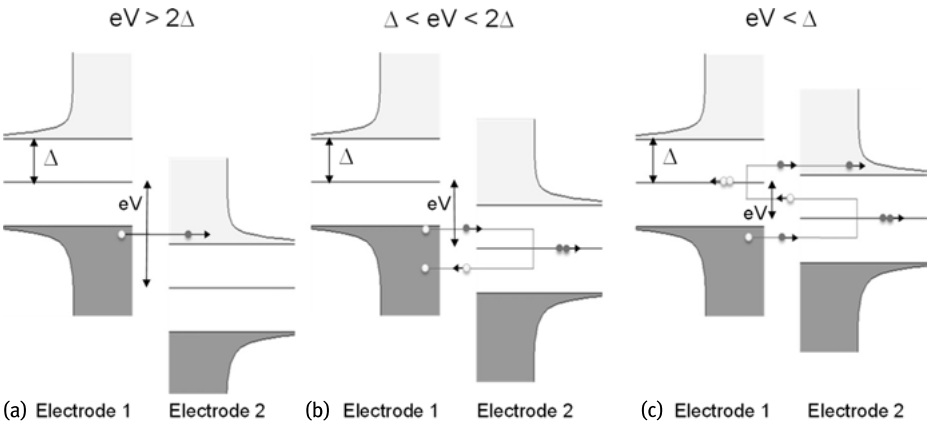

Fig. 1.5: In this image we show the behavior of a typical superconductor-superconductor junction when tip and sample are sufficiently close to show in-gap conductance. In (a) we show a single particle tunneling process for bias voltages above 2Δ. In (b) we show in-gap conductance due to a process crossing the tunneling barrier twice through Andreev reflection. In (c) we show the process crossing the tunneling barrier three times.

characteristics of N-S junctions for any tunneling barrier. An extension of the BTK formalism to superconductor-superconductor (S-S) junctions was later made by [37].

A more detailed analysis of the S-S situation takes into account all quasiparticle bound states. The formalism developed by [38, 39] leads to results that reproduce exactly the experimental observations in junctions involving a controlled amount of conduction channels. In Figure 1.5c we show schematically an example of multiple Andreev reflection processes. For $eV < 2\Delta$ multiple Andreev reflections occur in both electrodes 1 and 2. The smaller eV is compared to Δ, the larger is the number of Andreev reflections needed to obtain an Andreev current. For example, in the cases shown in Figure 1.5 we obtain one single quasiparticle transmitted in case (a), two in (b) – in the form of a Cooper pair, and three in (c) – in the form of a Cooper pair and an excited quasiparticle. For a current to flow from one junction to the other, the transmission probability must be multiplied at each barrier crossing. For a junction with transmission τ, the processes shown in Figure 1.5(b) and (c) have transmissions τ^2 and τ^3, respectively. Thus, unless τ is close to one, the contribution of Andreev reflection processes to the tunneling current is small. For a typical STM measurement in tunneling regime, with tunneling resistance of 10 MΩ, the transmission is about 10^{-3} ($\tau = (1/\sigma_0 \times 10\,\mathrm{M}\Omega)^{-1}$). It is thus difficult to observe Andreev reflection processes in the tunneling limit, although it is not impossible by measuring carefully enough and at short tip-sample distances, as discussed by [40].

With the STM we can control tip to sample distance, from high resistance tunneling conditions down to atomic contact between the electrodes (tip and sample). As the tip is moved towards the sample, the transmission through the tunnel barrier τ increases. In Figure 1.6 we present a series of current-voltage and conductance curves ($I - V$ and $dI/dV - V$) obtained when a Pb tip is moved towards a Pb sample. Similar results have been discussed by [34, 41]. We observe features in the curves for $V < 2\Delta$ when the resistance of the junction is decreased towards contact. Atomic contact is reached when the transmission equals a single quantum channel with spin degeneracy, $\tau = 1$, that is, when the resistance approaches the inverse of the quantum of conductance $1/\sigma_0 = R_\mathrm{Q} = h/2e^2 = 12.9\,\mathrm{k}\Omega$.

For a single quantum channel, each value of the transmission τ is uniquely locked to a single current versus bias voltage curve. Thus, from the experimental curves we can obtain, with high precision, the number of quantum channels and their transmission τ_i, as first shown by [32].

The conductance curves shown in Figure 1.6 also present a feature at zero bias. This feature is the signature of the Josephson effect due to Cooper pair tunneling between both electrodes. [42] calculated the critical current of the Josephson junction I_C in a short constriction at zero temperature and found $I_\mathrm{C} = (\pi\sigma_\mathrm{N}\Delta)/2e$, where σ_N is the conductance of the junction in the normal state. Its value for quantum contacts with a small number of conducting channels was calculated by [43]. Available experiments provide T_C values smaller than expected in calculations that usually do not take into account the actual properties of the junction, namely thermal broadening,

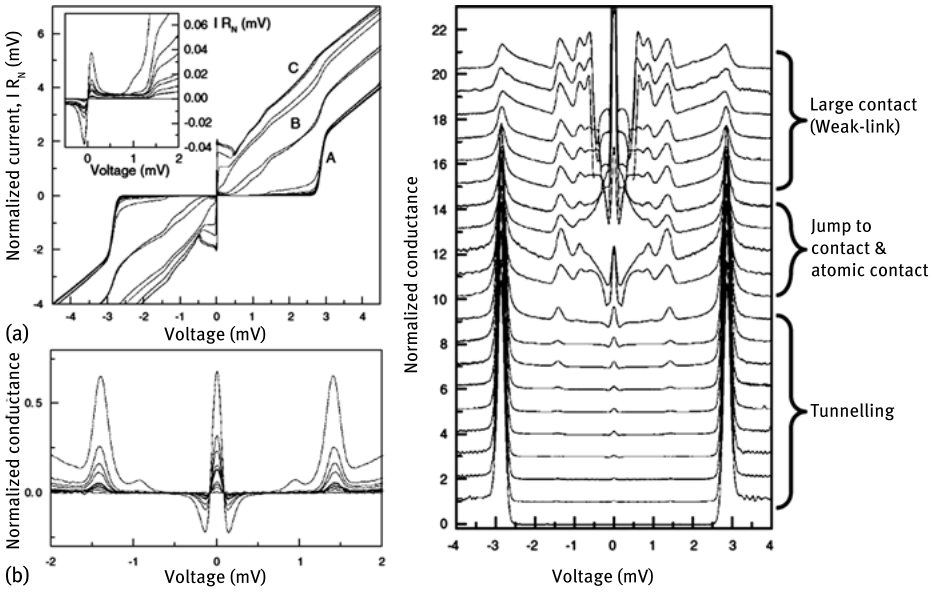

Fig. 1.6: Typical experimental results obtained using a superconducting tip and sample of the same material (Pb). In (a) we show the normalized current versus bias voltage curves. The inset shows the behavior close to zero bias, which clearly shows the Josephson effect. In the main figure, A, B and C provide sets of curves for different resistances of the junction (large contact, atomic size contact and tunneling, respectively). In (b) we show the tunneling conductance within the superconducting gap. In (c) we show the tunneling conductance in the three regimes A, B and C.

capacitance to ground and high frequency shunt. For instance, the Josephson current decreases considerably when the thermal energy $k_B T$ is above the Josephson coupling energy E_J. E_J is given by $E_J = \Delta h/(8e^2 R_N)$, where R_N is the junction's resistance and Δ the superconducting gap. When R_N is higher than 1 MΩ, E_J is of the order of an mK in most superconductors. If $E_J \approx k_B T$, the superconducting phase dynamics are dominated by thermal fluctuations and the Josephson current appears as a reduced peak centered at small finite voltage instead of a sharp zero bias feature. [44] could reduce phase slippage by increasing damping through resistors and capacitors located close to a break junction. However, this is difficult to implement in an STM set-up where the prime requirement is imaging. [45] recently analyzed electromagnetic coupling of the Josephson junction to high-frequency electromagnetic modes of the tip. This provides relevant clues to better understand the Josephson signal in an STM. More recent work by [46] uses a high T_c superconductor to increase the value of the critical current, combined with a method allowing us to measure the topography at high bias voltage and at the same time the Josephson signal in the I-V curves at much smaller bias voltages.

In summary, the tunneling conductance curves obtained using superconducting tips provide significant advantages in studying both superconducting and normal samples. In the tunneling regime, the conductance curves are considerably sharp-

ened at the bias voltage of the superconducting gap of the tip. For superconducting samples, there are additional features located at the bias voltage corresponding to the gap difference at finite temperatures. This improves measurements of the gap of the sample versus temperature. Coming closer to the contact regime, it is also possible to study Andreev reflection and the Josephson current as a function of the position.

1.2 Mapping the superconducting condensate at the length scales of the coherence length and below

1.2.1 Gap structure and atomic size tunneling

The tunneling conductance maps of a conventional s-wave superconductor are expected to be essentially featureless at zero magnetic field, because the superconducting gap is spatially homogeneous in the absence of vortices, currents or pair-breaking centers. However, STM experiments in many superconductors show tunneling conductance maps with atomic-scale features in the superconducting density of states.

To explain this we need to remember that atomic orbitals of tip and sample couple to provide the tunneling conductance in an STM. The tunneling matrix elements depend on the energy and vary with the atomic termination. If the superconducting gap varies strongly over the Fermi surface, the local variations in the tunneling matrix elements can modify the contribution of different parts of the Fermi surface to the tunneling density of states $N(E)$.

A first attempt to account for atomic-scale changes in the superconducting density of states of 2H-$NbSe_2$ was made by [11]. The Ansatz was a simple anisotropic superconducting gap and a spatially anisotropic tip. The anisotropic superconducting gap is found by using a tight-binding description of the electronic properties of 2H-$NbSe_2$ that captures a few basic properties of this material, such as a hexagonal Fermi surface with two sheets, one at the center of the Brillouin zone (Γ) and the other at the corners K and K' (Figure 1.7[a]). Only the Nb atomic orbitals are taken into account. Although the surface consists of Se atoms, it is expected that the main anisotropic features are related to the Nb atomic d orbitals. The considered orbitals are d_{xy} and $d_{x^2-y^2}$ that form two four-fold shapes rotated by 45°, as shown in Figure 1.7b. The anisotropy of the tip is modeled by an ellipse (Figure 1.7b). The angle between the long axis of the ellipse and the line joining the center of the ellipse and the atomic positions is θ_0.

When varying the position of the tip over the sample, θ_0 varies, resulting in an atomic size modulation of the density of states. The resulting density of states (Figure 1.7c) depends on the angle θ_0. The corresponding spatial modulation has a six-fold symmetry and is located in k-space at the atomic positions. The experiment indeed shows tunneling conductance maps with atomic size variations mainly at the bias voltages where the gap anisotropy produces a finite tunneling conductance. Thus, the energy dependence of the peaks of the Fourier transform of the conductance maps shows

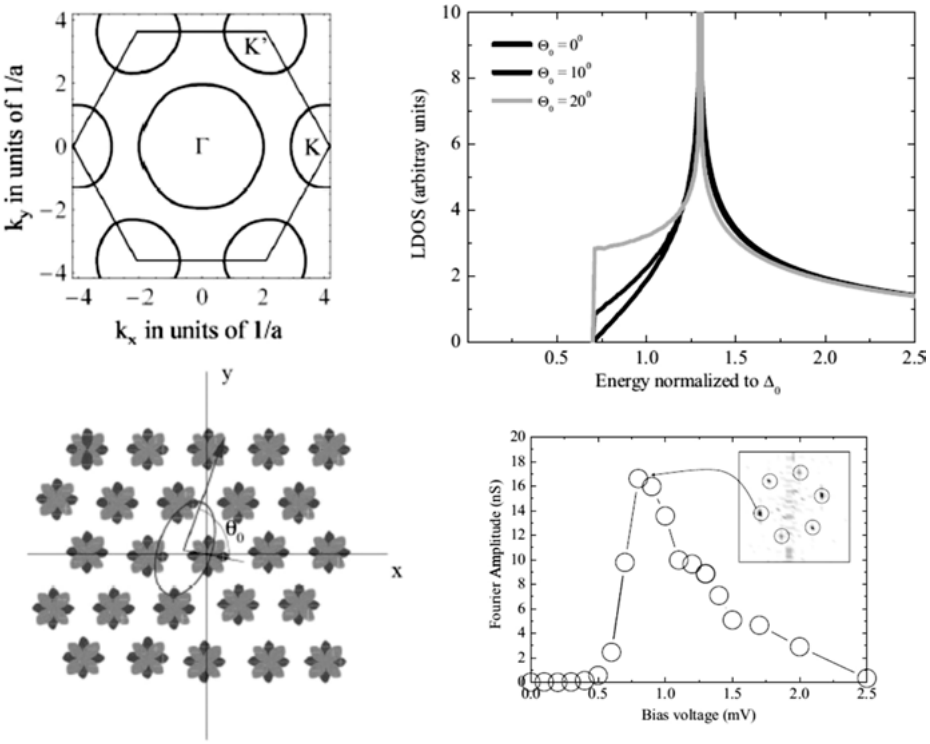

Fig. 1.7: In (a) we show a strongly simplified model for the Fermi surface of 2H-$NbSe_2$. In (b) we show main d-like atomic orbitals on the surface. The ellipse represents an anisotropically shaped tip, with a long axis turned by an angle θ_0 from the surface atomic lattice. In (c) we show the obtained local density of states as a function of the angle θ_0. In (d) we show the bias voltage dependence of the size of the six vortex lattice Bragg peaks from the Fourier transform of the tunneling conductance maps.

a maximum at these bias voltages. When comparing this variation (Figure 1.7[d]) with the results of the model (Figure 1.7[c]), we see that these qualitatively coincide – the largest spatial variation is found at the smaller gap edge.

A spatially anisotropic tip was also considered by [47]. These authors find that the tunneling conductance maps can show atomic size modulations revealing the spatial anisotropy of the electronic properties of the sample, such as those caused by electronic nematic order. They find that such modulations might disappear in the topographic maps. In the topographic maps, the feedback signal required to maintain a constant tunneling current over the surface is shown. That is, topographic maps provide maps of a quantity related to some extent to the current I at the bias voltage V. I is the conductance integrated from the Fermi level up to $E = eV$. Spatially varying features in the density of states that show some dependence on energy can be considerably reduced by the integration.

More recently, density functional theory calculations by [48] provide local densities of states that vary spatially at atomic size. The authors find that the decay of the tunneling current I with distance strongly varies depending on the contribution to I from different parts of the Fermi surface.

Present efforts aim at obtaining the connection between density functional calculations and variations in the contributions to the superconducting tunneling conductance.

1.2.2 Gap structure from Fermi sea oscillations

The scattering intensity of surface oscillations is also modified by the superconducting gap opening (Figure 1.8). The intensity can follow, in principle, the superconducting density of states, i.e., it increases at the gap edge and disappears within the superconducting gap. Tracing the oscillations with energy and momentum thus directly provides the reciprocal space structure of the superconducting gap. This has been done in several systems, including simple s-wave superconductors for example in Pb by [49], cuprates by [50] and heavy fermions by [51].

1.2.3 Gap structure and vortex shape

A vortex is a singularity at which the superconducting order parameter vanishes only at a single point in the plane perpendicular to the magnetic field. A vortex spans the reciprocal space gap structure into the real space, because the shape of the vortex depends on the size of the superconducting gap along the angular directions in the plane perpendicular to the magnetic field. In Figure 1.9, we schematically present one

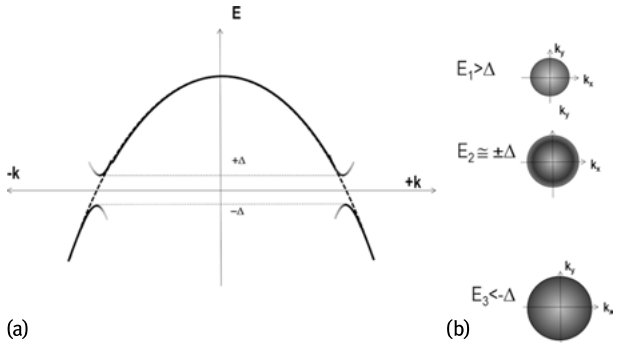

Fig. 1.8: In (a) we show schematically a hole band above (dashed line) and below (solid line) the superconducting transition temperature T_c. In (b) we show the Fourier transform of scattering surface waves on point impurities. Within the superconducting gap, scattering vanishes. At the quasiparticle peaks, the scattering wavevectors are spread and the intensity increased.

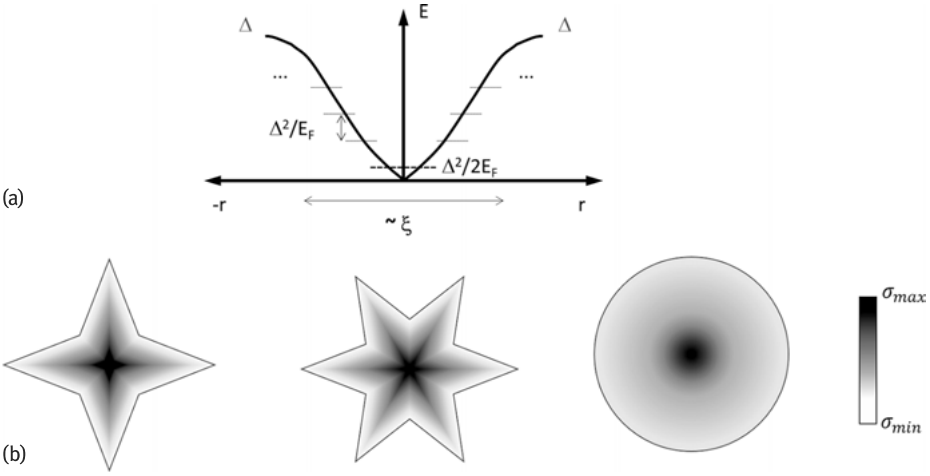

Fig. 1.9: In (a) we show a cartoon picture of the spatial variation of the superconducting order parameter as a function of the position in a vortex core (line). Andreev levels are marked as horizontal dashed lines. In (b) we show a cartoon of possible vortex core shapes. For materials with, from left to right, electronic properties with square, hexagonal and circular symmetry. The gray scale represents the conductance, with σ_{max} the conductance at the vortex core and σ_{min} the conductance outside the core.

particularly useful way to understand vortex cores. The Andreev reflection process occurs at any N-S interface. Inside a vortex, there is no "true" normal phase, just a point where the superconducting order parameter vanishes. However, the spatial variation of the superconducting order parameter allows the creation of Andreev states inside the vortex core (Figure 1.9). [52] first discussed these Andreev states. They form because of multiple Andreev reflections, in a similar way as the resonant states formed at an S-S junction discussed above. The circular symmetry of the vortex problem gives, however, a different distribution of theses states as a function of the position and the energy. [52] found that they are located at energies separated by $\frac{\Delta^2}{E_F}$ where Δ is the superconducting gap and E_F the Fermi energy. Measurements by [53] showed the energy levels as peaks in the density of states at the vortex core center. When going out of the vortex core, these peaks are shifted towards higher values, as expected by theory. The order of magnitude of the lowest lying level can be obtained by a simple zero point energy argument. One finds that $\epsilon_0 \approx \frac{\hbar\Delta}{2m\hbar v_F \xi} \approx \frac{\Delta}{2k_F\xi}$, with v_F the Fermi velocity and k_F the Fermi wavevector. We can then use the BCS relation $\xi = \frac{\hbar v_F}{\pi\Delta}$ to find $\epsilon_0 \approx \frac{\Delta^2}{2E_F}$.

In the presence of small amounts of scattering by impurities or defects, the vortex core states are not well defined and the density of states becomes featureless inside the vortex core. For not too large scattering, the density of states can be linked to the spatial dependence of the superconducting order parameter through a relation first found by de Gennes. Recently, this was used to find the spatial dependence of the order parameter in the vortex core. As shown by [54], the result is that the spatial variation of

the order parameter within a vortex is universal and does not depend on the particular properties of the material. This holds for two-band superconductors, in particular when interband scattering is strong.

1.3 Mapping the superconducting condensate at large scales

Vortex matter is the generally accepted denomination for the ensemble of quantized flux lines that forms in many superconductors when submitted to external magnetic fields. The existence of this matter was predicted theoretically by [55], which showed that flux lines distribute forming a lattice. Ten years later this lattice was visualized in magnetic decoration experiments by [56]. The first experiments showing large-scale vortex imaging by STM were made by [53] and showed a great deal of information on the structure and behavior of the vortex lattice. From these pioneering experiments, STM has evolved a lot. Now, the larger data acquisition rate and the development of new analysis methods has significantly increased the possibilities of this tool. Present day STM's can acquire topographic and conductance images of micrometric size in time scales ranging between a few seconds and minutes, with enough resolution to identify individual vortices. The challenge is now to push the working playground of the STM/S to the extreme conditions of high magnetic fields and very low temperatures.

Large-scale imaging in STM/S opens the door to study dynamic phenomena, like vortex melting and vortex creep, and to make quantitative statements about them by viewing individual behavior within the lattice or calculating statistically relevant correlation functions.

1.3.1 Techniques sensing the local magnetic field

The first large-scale vortex imaging was performed using techniques that measure the local magnetic field. As mentioned in the introduction, there are several reviews covering scanning probe techniques of the local magnetic field. Magnetic decoration and Lorentz microscopy are additional tools that have been widely used to study superconductors. Magnetic decoration consists of spreading magnetic particles on the surface of a superconductor subject to a small magnetic field and then viewing the positions of these particles using a scanning electron microscope (see for example [56, 57] or [58]). Lorentz microscopy uses the phase information of an electron wave transmitted through magnetic fields. It was developed by [59] to observe flux lines and dynamics of vortices in superconductors under magnetic fields. When a superconducting thin film under a magnetic field is slightly tilted from a normal incident electron beam (that is, a beam from a Transmission Electron Microscope), electrons passing through vortices in the film are deflected by the magnetic fields of the vortices. By sim-

ply defocusing the electron microscope image, the resulting pattern of the intensity of transmitted electrons shows vortices as circular spots of bright and dark contrast features. The time resolution is limited by the properties of the scanning electron beam. This tool was first used to study vortex dynamics by direct visualization.

When increasing the magnetic field, the magnetic overlap between vortices is usually very large. The intervortex distance a is given by $a \approx \frac{50}{\sqrt{H}}$ nm, with H in T. Thus, for fields of 100 Gauss, the intervortex distance is 500 nm. The penetration depth in many type II superconductors is of the order of this value or larger, so that magnetic imaging techniques usually lose their ability to view isolated vortices above a few hundreds of Gauss.

1.3.2 Introduction to the vortex lattice with STM

It is useful to start by making a comparison between atomic scale and vortex lattice measurements. In Figure 1.10a and b we show STM images of two isostructural dichalcogenides 2H-$NbSe_2$ and 2H-NbS_2. The atomic lattice observed by STM in these compounds is the chalcogen (Se or S) atomic lattice. These compounds consist of two $NbSe_2$ (or NbS_2) blocks separated by a van der Waals gap. The largest inter atomic distances occur between two layers of triangular chalcogen sublattices. The sample is prepared by exfoliation, which occurs at the van der Waals gap, so that the surface consists of the triangular chalcogen atomic lattices. In addition to the atomic lattices an atomic superstructure appears for 2H-$NbSe_2$ due to a charge density wave (insets in the right panels of Figure 1.10). This kind of additional modulation is a sort of a "trompe l'oeil" (or optical illusion) added to the atomic modulation in STM images. A trained eye can detect even weak modulations in STM images.

At the vortex center, we observe a strong zero bias peak in the tunneling conductance (left panels of Figure 1.10a and b). Its evolution with bias voltage when leaving the center of the vortex is similar in both compounds and follows the expected behavior for the Caroli de Gennes and Matricon states discussed above. The vortex core has a hexagonal shape in 2H-$NbSe_2$ due to the influence of the charge density wave in the in-plane shape of the superconducting gap.

Note that the observed differences in the shape of the vortices appear in the individual vortices but not in the lattices. Both are hexagonal, following the standard theoretical prediction, and both are oriented with the crystalline lattice.

We should note that these anisotropic dichalcogenides are easily exfoliable in situ at low temperatures. This has many advantages for STM, because the surface comes out clean and usually free of defects. Unfortunately, this is not always the case. To study superconductors with STM one needs high quality samples and in addition adequate sample surface handling and preparation methods. Sometimes, the surface can be stable under ambient conditions as for example in the work by [60] or [61], but this is not generally true.

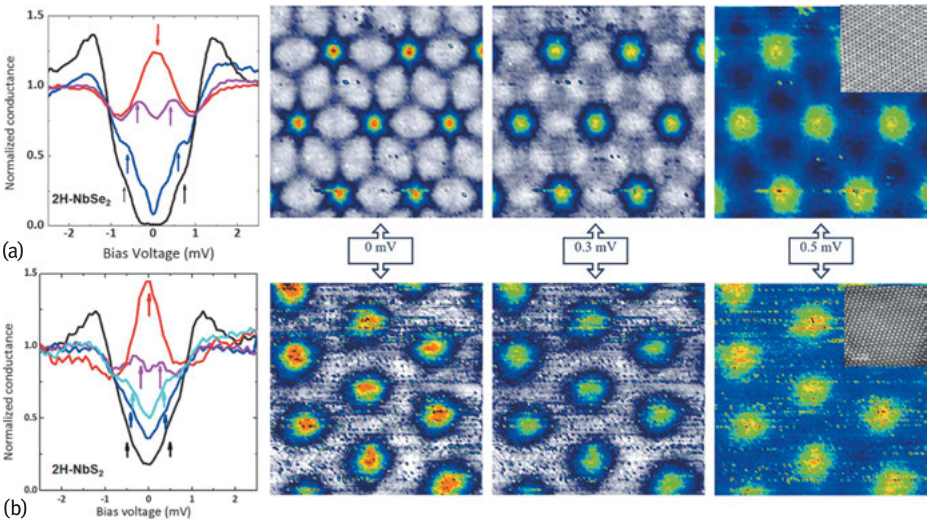

Fig. 1.10: In the left panels we show the tunneling conductance versus bias voltage when leaving the vortex center and in the rest of the panels we show vortex lattice images taken at different bias voltages. In (a) we show results in 2H-$NbSe_2$ and in (b) results in the isostructural 2H-NbS_2 at 0.1 K and 0.15 T. The bias voltage is marked for each image. In the insets of the right panels we show topographic images made in each compound. The color code is adjusted to provide the value of the conductance in each image and in the left panels, red is for vortex center and the other curves are taken roughly equidistantly until reaching the intervortex superconducting density of states. Arrows in the left panels mark the position of the Caroli de Gennes Matricon levels in each position. Image adapted from [62].

The investigation of vortex matter with STM/S in cuprate superconductors has been a challenge for several groups over the last decades (see the review of [12]). However, the lack of high quality single crystals was an important drawback for success in many cases. Today, it seems that this problem has been solved and there are groups that have access to excellent quality samples of these materials. It has been argued that the small coherence length enhances the negative effects of surface structural defects, impurities and contamination. However, these difficulties have been overcome by several groups and nearly the whole panoply of atomic-scale measurements, including Fermi surface, impurity-induced pair breaking, vortex core imaging and Josephson imaging has been made (see for instance work by [23, 46, 50, 63] and reviews by [12] and [14]). Vortex cores are particularly small. Moreover, vortex core states produce tunneling conductance curves quite similar to the tunneling conductance in between vortices. Thus, it remains very difficult to see vortices and to do large-scale vortex lattice maps in cuprates. Vortex cores usually provide features of larger sizes in other superconductors, often with larger coherence lengths, such as the nickel borocarbides, the iron-based superconductors or in thin films. These studies have been reviewed for example in [14] and [13].

1.3.3 Vortex lattice melting

Vortex lattice melting has been much discussed in cuprates, because their T_c is high and the Levanyuk–Ginzburg LG_i parameter large. LG_i is the ratio between the superconducting condensation energy and the critical temperature (see [64] and [65]). In high T_c superconductors, this ratio approaches one (contrasting values of the order of 10^{-5}–10^{-6} in usual low T_c superconductors), so that these materials are very sensitive to thermal fluctuations. As reviewed for example by [66], [67] or [68], in a large region of their temperature-magnetic field phase diagram, thermal energy becomes larger than elastic or pinning energies, producing thermally induced vortex motion. The formation of a vortex liquid suppresses the zero resistance state that makes superconductors so attractive for technological applications. That is why much effort has been invested to understand vortex lattice behavior across the melting transition through macroscopic transport and thermodynamic properties.

STM provides insight into the microscopic mechanism behind the formation of a vortex liquid through direct imaging. [69] imaged the melting transition of a two-dimensional (2D) vortex lattice in an amorphous superconducting thin film, showing a continuous three-step process with intermediate phases appearing before the formation of the isotropic vortex liquid. The observed behavior can be understood within the scenario described by the 2D melting theory developed by [70, 71], [72] and [73] (BKTNHY theory). The vortex images show the solid, hexatic and liquid phases expected within 2D melting. In addition, there is another intermediate phase characterized by the presence of smectic-like one-dimensional (1D) vortex arrangements that coexists with the hexatic phase just before the isotropic liquid is formed. Calculations of the vortex lattice melting in 2D superconductors (see [74]) also show such linear vortex arrangements.

STM images of isotropic vortex liquid do not give any spatial contrast and instead show a homogeneous value for the conductance as a function of the position, because thermally induced vortex motion is much faster than the scanning rate of the STM. Images of the liquid are featureless and are difficult to distinguish from images of the normal phase. As shown in Figure 1.11, to identify the isotropic liquid, authors compare the temperature dependence of the spatially averaged normalized conductance at zero bias with the amplitude of the Bragg peaks in the Fourier transform of the tunneling conductance maps. Before the formation of the isotropic vortex liquid, vortex positions are identified in the conductance maps as usual, by tracing the zero bias conductance as a function of the position. The corresponding Fourier transform shows Bragg peaks with nonzero amplitude. With increasing temperature, the normalized conductance at zero bias outside vortex cores continuously increases due to thermal broadening. As a consequence, the spatially averaged conductance value increases while the Fourier amplitude of the Bragg peaks decreases. In the isotropic liquid phase, conductance maps show no contrast at all giving zero Fourier amplitude. Still, we find a superconducting signal in the tunneling data (upper right panel in Fig-

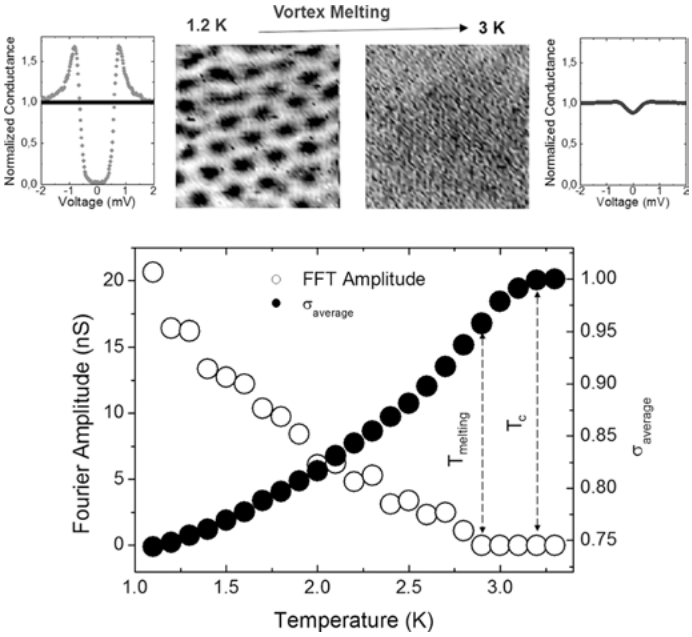

Fig. 1.11: Main panel shows the temperature dependence of the spatially average tunneling conductance at zero bias (black circles) and the amplitude of Bragg peaks appearing in the Fourier transforms of vortex images (empty circles). Vertical dashed arrows show the position where the formation of isotropic vortex liquid ($T_{melting}$) and normal state (T_c) occurs. Upper left panels show a vortex image before the formation of the isotropic vortex liquid at 1.2 K and the corresponding tunneling conductance found inside (black) and outside (gray) vortex cores. Right upper panels show a conductance map obtained in the isotropic liquid phase at 3 K and the tunneling conductance curve observed over the whose area.

ure 1.11). The isotropic liquid is then identified as the temperature range where the zero bias conductance is below the value of the normal phase but the Fourier amplitude in the conductance maps is zero at the position of the vortex lattice Bragg peaks.

Of relevance is also the direct visualization of vortex de pinning. [69] showed that, when increasing temperature in a vortex lattice distorted at 0.1 K due to pinning, the lattice becomes more ordered well below the melting temperature. Thermally activated vortex motion is thus important to understand the behavior of the vortex lattice in a large part of the phase diagram.

1.3.4 Vortex lattice creep

Distorted vortex lattices at 0.1 K show, however, practically no thermal motion. At such low temperatures, two orders of magnitude below T_c, the balance between elastic energy and pinning determines the static and dynamic behavior of the vortex lat-

tice. STM directly visualizes this competition, and can be used to identify elastic and plastic vortex motion. To produce vortex motion, a Bean critical state can be generated in a zero field cooled sample (magnetic field is applied at low temperatures). One can then produce vortex motion by subsequently changing the magnetic field in very small steps.

In a pioneering work, [75], unveiled the dynamical behavior of the lattice in irradiated and pristine samples of 2H-$NbSe_2$. This work was made at 4.2 K, so that temperature still played an enormous role. However, some features relevant to the competition between pinning and elastic energies were identified. In irradiated samples, the disordered lattice has a few vortices that are strongly pinned to the defects produced by irradiation. When changing the magnetic field, vortex motion sets in. Pinned vortices remain static, but the vortices in-between them flow, highlighting plastic deformation of the lattice. The deformation is anisotropic, following the local orientation of the vortex lattice. By contrast, pristine samples of 2H-$NbSe_2$ show much more continuous changes of vortex positions. The lattice moves along the direction of one of it's main axes. There is a periodic modulation in the longitudinal velocity with a frequency corresponding to the time needed to travel a distance equal to the intervortex distance a_0 (Figure 1.12). This is the so-called washboard frequency. It shows that the periodic vortex lattice is driven through randomly disordered pinning centers, see [77].

More recently, similar experiments were made in a 2D vortex lattice in an amorphous superconducting thin film at 100 mK (see [76]). In this work the pinning disorder was provided by variations in the sample's thickness which produce changes in vortex energy per unit length. The pinning centers were not point like, but modu-

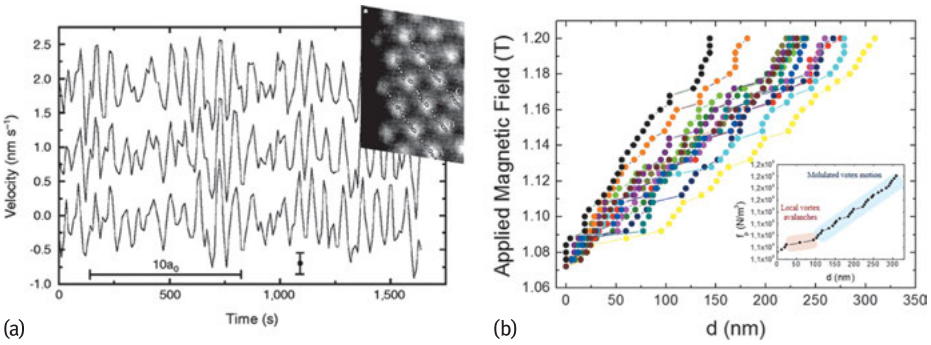

Fig. 1.12: a) (Figure adapted from [75]) Longitudinal velocity of the vortices shown in the upper right panel. The velocity oscillates as a function of time with period a_0. Data are taken in a pristine 2H-$NbSe_2$ single crystalline sample. b) Magnetic field versus accumulated distance of 12 vortex trajectories in an amorphous W-based thin film, data from [76]. The lower bottom inset shows the distance dependence of the pinning force $f_p = J_c B$, where J_c is the critical current density. Authors distinguish two types of vortex motion: modulated vortex motion (shading in blue) where vortices travel small distances following paths modulated with lattice periodicity and small vortex avalanches (shading in red) consisting of collective large jumps producing vortex rearrangements.

lations of the thickness along disordered, meander-like lines. The hexagonal lattices were slightly distorted and oriented in such a way as to conform to the immediate surrounding of linear pinning centers. Vortices close to linear pinning centers moved along them. Vortices in between pinning centers moved in bundles. The motion was well defined. Individual vortex trajectories showed that vortices travel small distances while the bundle becomes gradually distorted. Here, the vortex paths are modulated with the lattice periodicity due to a washboard potential, similar to the case of pristine 2H-$NbSe_2$ discussed above. Motion continued until the lattice got very distorted. The accumulated stress was then suddenly released through large collective jumps, which produced rearrangements of the vortex positions and gave a more ordered vortex lattice. Authors identified two different processes. A continuous periodic motion in which stress is accumulated at each step of the magnetic field, distorting the lattice within the hexagonal bundles. And plastic motion through small vortex avalanches that release stress.

1.3.5 Commensurate to incommensurate transitions in nanostructured superconductors

A particular case of vortex pinning occurs in the presence of periodic pinning centers. This kind of pinning is relevant when the intervortex distance a_0 is of the same order as the period of the pinning landscape d. The vortex lattice is commensurate to the periodic structure when a vortex lattice parameter is an integer multiple of the period of the pinning landscape. In this situation the lattice is generally ordered and free from topological defects. Conversely, the lattice is incommensurate to the periodic pinning centers when no lattice parameter is an integer multiple of the periodic pinning landscape. This might occur when both lattices are rotated to each other by an angle that is not related to the main symmetry properties of each lattice (that is, 180° for the linear array and 60° for the hexagonal vortex lattice). Incommensurate lattices are generally disordered. The amount of disorder depends on the strength of the periodic pinning potential. When the pinning potential is strong, groups of dislocations form along the linear features, separated by d. In weak pinning potentials, the disorder might be distributed over the whole vortex lattice. Commensurate to incommensurate transitions appear when a_0 is changed by varying the magnetic field. These considerations are generic to any combination of an elastic periodic lattice embedded in a periodic pinning potential and have been analyzed in totally different fields, such as colloids and optical lattices.

Over the last decades, a number of experimental and theoretical works have studied the response of the vortex lattice in the presence of periodic nanostructures with periodic arrangements of different symmetries, square or triangular. Nanostructures with different features such as holes or dots and shapes such as triangles, squares, hexagons or circles have been analyzed (see e.g., [79]). One-dimensional (1D) linear

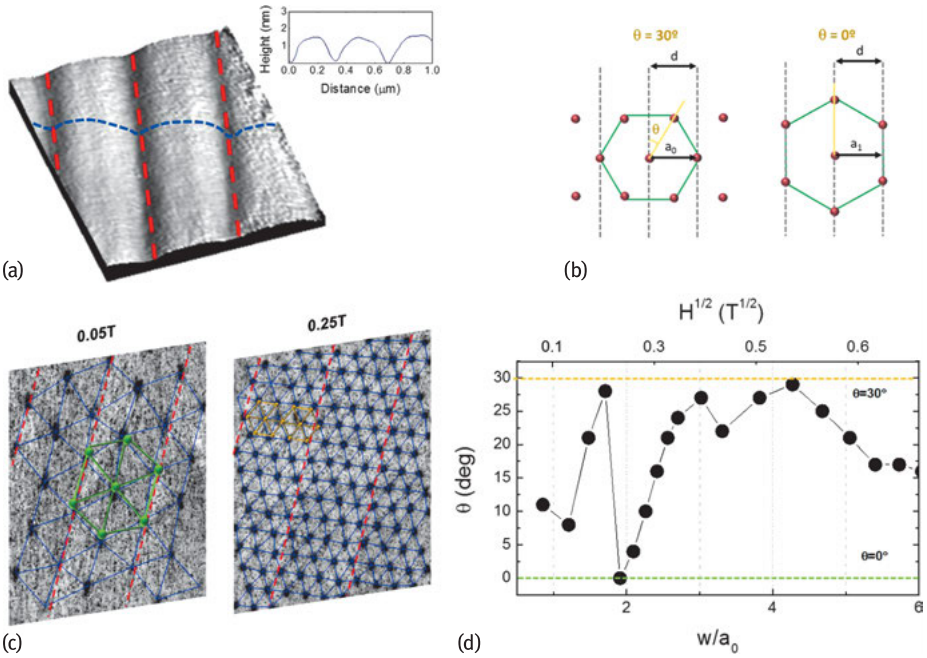

Fig. 1.13: (a) STM topography of a $1 \times 1.2\ \mu m^2$ area of the nanostructured thin film. Red dashed lines indicate the 1D modulation and inset shows the height profile along the blue dashed line. (b) Two main configurations of the hexagonal vortex lattice to the 1D linear potential. The angle defined between one main axis of the vortex lattice and the direction of the 1D linear nanostructure θ changes from 0° (right panel) to 30° (left panel). These provide, respectively, $d = ma_0$ and $d = n\sqrt{(3)}a_0/2$ with m, n integers, d the period of the 1D modulation and a_0 the intervortex distance. The figure shows the $m = 1$ (right) and $n = 1$ (left) cases. (c) Vortex lattice images taken in the area shown in (a) showing commensurate configurations of the vortex lattice to the 1D surface modulation with $n = 1$ at 0.05 T (left) and $m = 5$ at 0.25 T (right). Blue lines are the Delaunay triangulation. (d) Magnetic field dependence of θ at fields below 0.5 T. The vortex lattice oscillates between main commensurate configurations shown in (b) with $\theta = 0°$ and $\theta = 30°$. Figures adapted from [78].

modulations have been comparatively less studied. These are among the most interesting cases because it is easy to control the orientation of the vortex lattice and the ratio between the intervortex distance and the period of the potential. [80] define the commensurability ratio p as $p = d/a_0$, and the relative orientation between them, given by the angle θ. Both parameters govern the coupling strength between the vortex lattice and the 1D modulation.

So far it has remained very difficult to image vortex lattices in periodic pinning potentials, because surface quality and corrugation modified the pinning landscape away from the nanostructured geometries. [78] succeeded in creating a vortex lattice in a well-defined 1D potential. The vortex lattice was imaged as a function of the magnetic field using STM. There are no additional pinning centers in their amorphous

superconducting thin film. The sample is grown using the focus ion beam (FIB) deposition technique and the 1D potential is provided by a smooth surface corrugation created by the FIB during the fabrication process. The surface corrugation is below 1% of the total sample thickness and has a period of 400 nm (Figure 1.13a). Authors of this work find that the smooth 1D modulation of the thickness (red dotted lines in Figure 1.13) acts as an effective pinning center in the low-field region ($H < 0.4\,\mathrm{T} = 0.06H_{c2}$) where the commensurability ratio p is below 5. Between 0.01 T and 0.4 T, the orientation of the vortex lattice with respect to the linear surface modulation, θ, changes as a function of the field. The lattice rotates between two configurations at $\theta = 0°$ and $\theta = 30°$ that correspond, respectively, to matching conditions of the lattice to the linear pinning potential given by $d = n\sqrt{3}a_0/2$ and $d = ma_0$, with n and m being integers. A sketch of the configurations for $m = n = 1$ is shown in Figure 1.13b. In the vortex lattice images authors identify, at some particular fields, vortex configurations that clearly fulfil the matching conditions of the lattice to the periodic surface landscape. For example, at 0.05 T the lattice is oriented parallel to the 1D modulation with the intervortex distance satisfying $d = n\sqrt{3}a_0/2$ for $n = 2$ (green hexagon in Figure 1.13c, left panel). Whereas, at 0.25 T, $\theta = 30°$ with $d = ma_0$ for $m = 4$ (yellow hexagons in Figure 1.13c, right panel). The discrete changes between the two stable low-energy configurations at $\theta = 0°$ and $\theta = 30°$ are observed at the lowest fields. In Figure 1.13c we show the magnetic field dependence of the relative orientation between the lattice and the 1D potential given by the angle θ. Above 0.05 T, the lattice does not re-orient sharply but its orientation oscillates smoothly. At higher fields, above 0.4 T, the pinning due to the surface corrugation becomes negligible, because a_0 becomes much smaller than d, $a_0 \ll d$ and the elastic energy of the lattice dominates the pinning potential.

1.3.6 Order-disorder transition

Very often, at high magnetic fields and/or high temperatures, close to the H_{c2} line, the vortex lattice disorders. The order-disorder transition is connected to the softening of the vortex lattice. The magnetic field becomes nearly homogeneous, so that the strength of the intervortex interaction (which is of magnetic origin, see for example [35]) decreases close to the H_{c2} line. Then, the pinning strength overcomes the vortex-vortex repulsive interaction and vortices adapt their position to the disordered arrangement of pinning centers. A complete description of the order-disorder transition requires visualizing a large number of vortices at high magnetic fields, an ideal playground for STM.

An important tool to quantify the degree of disorder in the vortex lattice is the Delaunay triangulation (left panel in Figure 1.14a). It provides the bonds joining first neighbors giving for each vortex its coordination number. In a perfect hexagonal lattice, all vortices have six first neighbors, i.e., they all have a coordination number

equal to 6. Vortices with a coordination number different from 6 are defects of the perfect hexagonal vortex lattice. The most common defects are isolated 5-fold or 7-fold vortices, called disclinations, and bound pairs of them, called dislocations. A quantitative description of the disorder in the vortex lattice can be found by calculating the translational and orientational correlations functions, $G_K(r)$ and $G_6(r)$ (right panels in Figure 1.14a). These quantify the distance dependence of the weakening of, respectively, translational and orientational correlations in the vortex positions. $G_K(r)$ and $G_6(r)$, are defined from the translational and orientational order parameters, $\Psi_K(r)$

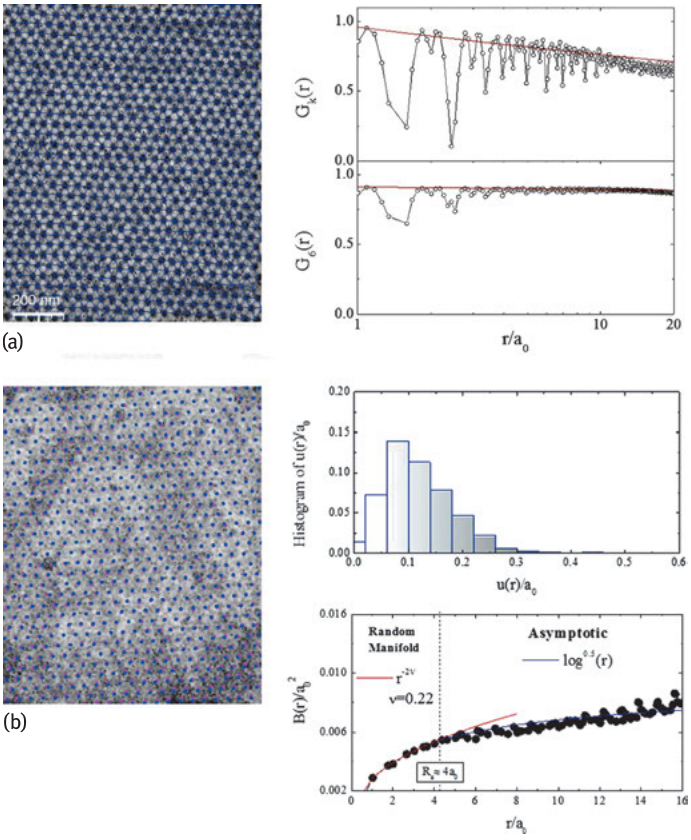

Fig. 1.14: (a) Left panel shows Delaunay triangulation of a vortex lattice image taken at 1.2 T in the region shown in Figure 1.13a. Right panel shows positional and orientational correlation functions, $G_K(r)$ and $G_6(r)$. Red lines are fits to power law decays. (b) Actual vortex positions obtained from (a) (magenta) and the calculated perfect hexagonal lattice (blue). The perfect hexagonal lattice has been rotated and translated to minimize the average mean square deviation with respect to the measured vortex lattice (see text for details). The gray scale corresponds to the spatial variations of the relative displacement between them, $u(r)$. This changes according to the histogram shown in the top right panel of (b). Bottom right panel of (b) shows the relative displacement correlator $B(r)$. Red and dark lines are fits as described in the text.

and $\Psi_6(r)$, as

$$G_K(r) =< \Psi_K(r)\Psi_K^*(0) >= \frac{1}{6}\sum_{l}^{6}\frac{1}{n(r)}\sum_{i,j}^{n(r)}\Psi_{K_l}(r_i)\Psi_{K_l}^*(r_j)\,, \tag{1.2}$$

$$\Psi_{K_l}(r_i) = e^{i\boldsymbol{K_l}\boldsymbol{r_i}}\,, \tag{1.3}$$

$$G_6(r) =< \Psi_6(r)\Psi_6^*(0) >= \frac{1}{n(r)}\sum_{i,j}^{n(r)}\Psi_6(r_i)\Psi_6^*(r_j)\,, \tag{1.4}$$

$$\Psi_6(r_i) = \frac{1}{n_{\mathrm{N}}^i}\sum_{k}^{n_{\mathrm{N}}^i} e^{i6\theta(r_{ik})}\,, \tag{1.5}$$

where r is the distance of any lattice site to the origin, $n(r)$ is the number of vortex pairs separated by a distance r, n_{N}^i is the number of the nearest neighbors of the vortex i as given by the Delaunay triangulation, $\boldsymbol{K_l}$ stands for each of the six main reciprocal lattice vectors and $\theta(r_{ik})$ is the angle of the nearest-neighbors bond between vortices i and j with respect to the reference axis. The six main reciprocal lattice vectors $\boldsymbol{K}$ are given by the position of the Bragg peaks in the Fourier transforms of the vortex lattice images.

The envelope of $G_K(r)$ and $G_6(r)$ for a perfect hexagonal lattice is equal to 1 and independent of the distance. The presence of defects in the lattice, such as dislocations or disclinations, produces a decay with r. Slow decay following a power-law dependence evidences quasi-long range order. Fast exponential decaying correlations evidence short range order.

The relative displacement correlator $B(r)$ is defined as $B(r) = \langle[\mathbf{u}(\mathbf{r}) - \mathbf{u}(\mathbf{0})]^2\rangle/2$. $\mathbf{u}(\mathbf{r}) = \mathbf{r} - \mathbf{r_p}$ is the displacement of each vortex at $\mathbf{r}$ relative to its position in the perfect lattice $\mathbf{r_p}$. Within a Gaussian disorder potential, $B(r)$ is related to $G_K(r)$ by $B(r) = e^{-K^2B(r)/2}$.

To calculate $B(r)$ requires generation of a perfect hexagonal lattice. This is compared to the real vortex arrangements so that deviation between them given by $\langle|\mathbf{u}(\mathbf{r})|^2\rangle$ is minimized with respect to translation and rotation to obtain the best match between the two arrangements. Figure 1.14b (right panel) shows the real vortex positions (magenta) and the calculated perfect hexagonal lattice that minimized deviations with respect to them (blue) for the vortex lattice image shown in Figure 1.14a. The positions for the perfect lattice obtained after minimization are used to compute the histograms and maps of the relative displacement, $u(r)$, shown, respectively, in the right panel and as the color code in the map shown in the left panel. The relative displacement correlator $B(r)$ is shown in the bottom inset in Figure 1.14b. The distance dependence of $B(r)$ is used to distinguish among different possible crossover effects when increasing distance. Generally speaking, at short distances we find the random manifold regime with $B(r) \sim r^{-2\nu}$. Here vortices explore many minima in the energy landscape but do no compete against each other, i.e., each vortex sees an independent random potential. At larger distances the vortex periodicity starts to play a role, and

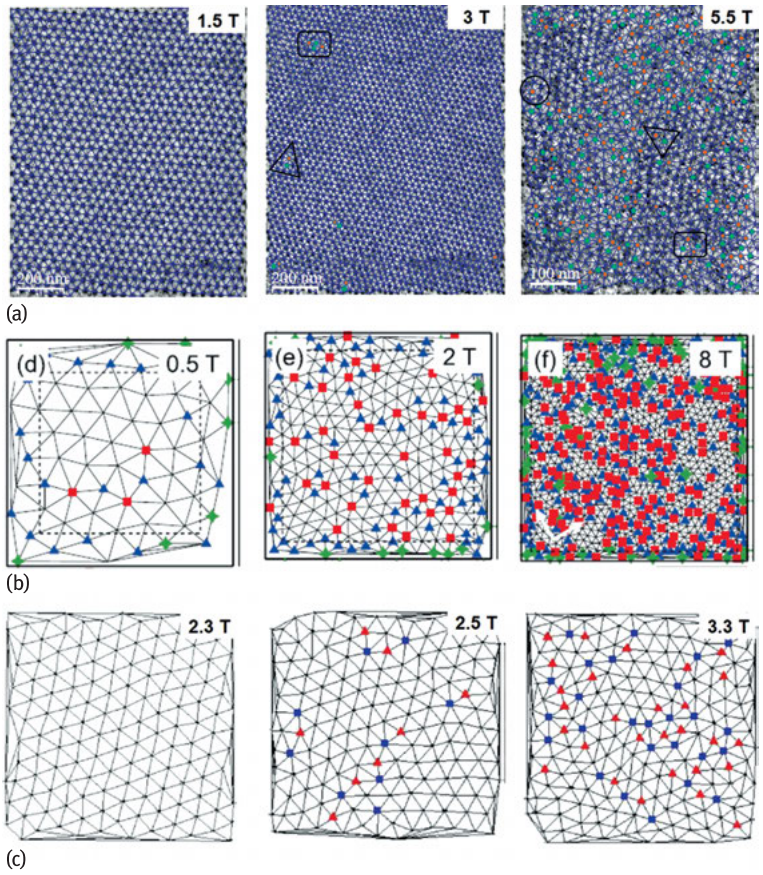

Fig. 1.15: (a) Vortex lattice images obtained in an amorphous superconducting thin film at 0.1 K. Vortices with five and seven nearest neighbors are identified by green and orange points. Dislocations formed by five and seven nearest neighbor pairs of vortices are identified by black triangles, pairs of dislocations by black rectangles and isolated disclinations by black circles. Figure adapted from Ref.[78]. (b) Vortex lattice images obtained in LiFeAs at 1.5 K. Vortices with five nearest neighbors are marked by blue triangles, with seven nearest neighbors by red squares and others by green stars. Figure adapted from [81]. c) Vortex lattice images obtained in $Co_{0.012}NbSe_2$ at 1.8 K. Triangles are vortices with five nearest neighbors and squares with seven. Figure adapted from [82].

$B(r)$ grows more slowly following a logarithmic dependence in the so-called asymptotic regime. The exponents characterizing the dependence of $B(r)$ in the different regimes depend on the type of disorder and the dimensionality of the vortex lattice.

The work of [78] characterizes the order-disorder transition in detail for a 2D vortex lattice. The disorder potential is not due to pinning centers, but to scale-invariant quasi-random potential from the correlations resulting from an incommensurate arrangement of the vortex lattice and the 1D modulation.

Figure 1.15a shows three representative vortex lattice images obtained across the transition. The ordered vortex lattice at low fields becomes gradually disordered when increasing the magnetic field. Authors find that the transition occurs in two steps and determine the critical exponents from the distance dependence of correlation functions directly obtained from the vortex positions. Uncorrelated long-range disorder produced by the linear surface corrugation drives the transition. For the first time, the local disorder potential and the disorder in the vortex lattice have both been identified separately using STM imaging.

The order-disorder transition has been also observed in crystalline superconductors. The origin for the disorder potential could not be determined and is probably pinning by randomly distributed impurities or defects. Figure 1.15b and c show triangulated vortex lattices as a function of magnetic field in, respectively, LiFeAs by [81] and $Co_{0.012}NbSe_2$ by [82]. In LiFeAs, disorder in the lattice might be produced by native defects in the crystalline structure when the lattice softens close to H_{c2}. In $Co_{0.012}NbSe_2$, disorder in the vortex lattice images is correlated with macroscopic magnetization measurements.

1.4 Conclusions

The STM is useful to understand relevant concepts of condensed matter physics by making vivid and visual images. It is a looking glass into a landscape that provides insight by showing electronic behavior at length scales from atomic to the macroscopic regime. Incrementing the amount of data points in images is one of the key issues to obtain such an insight. Another one, providing access to electronic behavior, is to do microscopy in a controlled very low-temperature environment.

We have shortly reviewed how to obtain atomic-scale information about the superconducting gap by using atomic-scale spectroscopy and spectroscopy on electronic wavefunctions scattered by defects. We have then shown the results obtained at scales of the order of the superconducting coherence length, highlighting the appearance of localized states inside vortex cores. Finally, we have addressed the features of the vortex lattice up to micron length scales and have given techniques needed to analyze large-scale images of vortex matter.

We consider that one relevant challenge is now to control, in situ, the electronic properties of the sample. For example, to be able to tune a superconductor through a quantum phase transition by measuring as a function of the magnetic field or by applying a gate voltage – and explore the multiple length scales expected in there.

Another relevant challenge is to obtain real-time visualization of ultrafast processes. This can be seen as quite far fetched today. We believe however that it might be possible to design pump-probe like STM experiments for low temperatures. Such experiments can provide real-time imaging of vortex motion or electronic relaxation.

Acknowledgment: We acknowledge discussions with A. Fente, E. Herrera, J. Benito, F. Martín, V. Barrena, Th. Grellmann and J.A. Galvis. We also acknowledge in depth discussions with A.I Buzdin, V.G. Kogan and F. Guinea. We particularly acknowledge the EU program Cost MP-1201 for long-term support and inspiration. The work was supported by the Spanish Ministry of Economy and Competitiveness (FIS2014-54498-R, MDM-2014-0377) and by the Comunidad de Madrid through programs Nanofrontmag-CM and MAD2D-CM (S2013/MIT-2850 and P2013/MIT-3007). IG acknowledges support from Axa Research Fund, FBBVA, FP7-PEOPLE-2013-CIG 618321 and the European Research Council (Grant 679080). We acknowledge Banco Santander and SEGAINVEX at UAM.

Bibliography

[1] Wolf EL. Principles of Electron Tunneling Spectroscopy. Oxford University Press, Oxford, 1989.
[2] Binnig G, Rohrer H, Gerber Ch, Weibel E. Tunneling through a controllable vacuum gap. Appl.Phys. Lett. 40:178, 1982.
[3] de Lozanne AL, Elrod SA, Quate CF. Spatial variations in the superconductivity of Nb_3Sn measured by low temperature tunneling microscopy. Phys. Rev. Lett. 54:2433, 1985.
[4] Kirtley JR, Tsuei CC, Park SI, Chi CC, Rozen J, Shafer MW. Local tunneling measurements of the high-Tc superconductor $La_{2-x}Sr_xCuO_{4-y}$. Phys. Rev. B 35:7216, 1987.
[5] Vieira S, Ramos MA, Vallet-Regi M, Gonzalez-Calbet JM. Tunneling measurements of the energy gap in $Bi_4Ca_2Sr_3Cu_4O_{16+\delta}$. Phys. Rev. B 38:9295, 1988.
[6] Hess HF, Robinson RB, Dynes RC, Valles JM, Waszczak JV. Scanning-Tunneling-Microscope observation of the Abrikosov flux lattice and the density of states near and inside a fluxoid. Phys. Rev. Lett. 62:214, 1989.
[7] Binnig G, Quate CF, Gerber Ch. Atomic force Microscope. Phys. Rev. Lett. 56:930–933, 1986.
[8] Kirtley JR. Fundamental studies of superconductors using scanning magnetic imaging. Rep. Prog. Phys. 73:126501, 2010.
[9] Nanoscience and engineering in superconductivity, Eds Moshchalkov VV, Wordenweber R, Lang W. , 2010.
[10] Bending SJ. Local magnetic probes of superconductors. Adv. in Phys. 48:449, 1999.
[11] Guillamón I, Suderow H, Guinea F, Vieira S. Intrinsic atomic-scale modulations of the superconducting gap of 2H-$NbSe_2$. Phys. Rev. B 77:134505, 2008.
[12] Fischer O, Kugler M, Maggio-Aprile I, Berthod C. Scanning tunneling spectroscopy of high-temperature superconductors. Rev. Mod. Phys. 79:353, 2007.
[13] Hoffman JE. Spectroscopic scanning tunneling microscopy insights into Fe-based superconductors. Rep. Prog. Phys. 74:124513, 2011.
[14] Suderow H, Guillamon I, Rodrigo JG, Vieira S. Imaging superconducting vortex cores and lattices with a scanning tunneling microscope. Superc. Sci. Technol. 27:063001, 2014.
[15] Tersoff J, Hamann DR. Theory and application for the scanning tunneling microscope. Phys. Rev. Lett. 50:1998, 1983.
[16] Tersoff J, Hamann DR. Theory of the scanning tunneling microscope. Phys. Rev. B 31:805, 1985.
[17] Chen CJ. Introduction to Scanning Tunneling Microscopy. Oxford University Press, New York, 1993.
[18] Ziman JM. Principles of the theory of solids. Cambridge University Press, Cambridge, 1995.

[19] Petersen L, Sprunger PT, Laegsgaard E, Hofmann Ph, Briner BG, Doering M, Rust H-P, Bradshaw AM, Besenbacher F, Plummer EW. Direct imaging of the two-dimensional Fermi contour: Fourier-transform STM. Phys. Rev. B 57:R6858, 1998.
[20] Simon L, Bena C, Vonau F, Cranney M, Aubel D. Fourier-transform scanning tunnelling spectroscopy: the possibility to obtain constant-energy maps and band dispersion using a local measurement. J. Phys. D 44:464010, 2011.
[21] Pascual JI, Dick A, Hansmann M, Rust HP, Neugebauer J, Horn K. Bulk electronic structure of metals resolved with scanning tunneling microscopy. Phys. Rev. Lett. 96:046801, 2006.
[22] Allan MP, Chuang T-M, Massee F, Yang Xie, Ni N, Bud'ko SL, Boebinger GS, Wang Q, Dessau DS, Canfield PC, Golden MS, Davis JC. Anisotropic impurity states, quasiparticle scattering and nematic transport in underdoped $Ca(Fe_{1-x}Co_x)_2As_2$. Nat. Phys. 9:220, 2013.
[23] Hoffman JE, McElroy K, Lee D-H. and et al. Imaging quasiparticle interference in $Bi_2Sr_2CaCu_2O_{8+\delta}$. Science 297:1148, 2002.
[24] Weismann A, Wenderoth M, Lounis S, Zahn P, Quaas N, Ulbrich RG, Dederichs PH, Blügel S. Seeing the Fermi surface in real space by nanoscale electron focusing. Science 323:1190, 2009.
[25] Fano U. Effects of configuration interaction on intensities and phase shifts. Phys. Rev. B 124:1866, 1961.
[26] Crommie MF, Lutz CP, Eigler DM. Imaging standing waves in a two-dimensional electron gas. Nature 363:524, 1993.
[27] Franke KJ, Shulze G, Pascual JI. Competition of superconducting phenomena and Kondo screening at the nanoscale. Science 332:940, 2012.
[28] Hamidian MH, Schmidt AR, Firmo IA, Allan MP, Bradley P, Garrett JD, Williams TJ, Luke GM, Dubi Y, Balatsky AV, Davis JC. How Kondo-holes create intense nanoscale heavy-fermion hybridization disorder. Proc. Nat'l. Acac. Sci USA 8:18233, 2011.
[29] Schmidt AR, Hamidian MH, Wahl P, Meier F, Balatsky AV, Garret JD, Luke GM, Davis JC. Imaging the Fano lattice to 'hidden order' transition in URu_2Si_2. Nature 465:570, 2010.
[30] Ernst S, Kirchner S, Krellner C, Geibel C, Zwicknagl G, Steglich F, Wirth S. Emerging local Kondo screening and spatial coherence in the heavy-fermion metal $YbRh_2Si_2$. Nature 474:362, 2011.
[31] Maldonado A, Suderow H, Vieira S, Aoki D, Flouquet J. Temperature dependent tunneling spectroscopy in the heavy fermion $CeRu_2Si_2$ and in the antiferromagnet $CeRh_2Si_2$. J. Phys.: Condens. Matter 24:475602, 2012.
[32] Scheer E, Agraït N, Cuevas JC, Levy-Leyati A, Ludolph B, Martín-Rodero A, Rubio-Bollinger G, van Ruitenbeek JM, Urbina C. The signature of chemical valence in the electrical conduction through a single-atom contact. Nature 394:154, 1998.
[33] Agraït N, Levy Yeyati A, van Ruitenbeek JM. Quantum properties of atomic-sized conductors. Physics Reports 377:81–279, 2003.
[34] Rodrigo JG, Suderow H, Vieira S, Bascones E, Guinea F. Superconducting nanostructures fabricated with the scanning tunnelling microscope. J. Phys.: Condens. Matter 16:1151, 2004.
[35] Tinkham M. Introduction to Superconductivity. McGraw International, Singapore, 1996.
[36] Blonder GE, Tinkham M, Klapwijk TM. Transition from metallic to tunneling regimes in superconducting microconstrictions: Excess current, charge imbalance, and supercurrent conversion. Phys. Rev. B 25:4515, 1982.
[37] Octavio M, Tinkham M, Blonder GE, Klapwijk TM. Subharmonic energy-gap structure in superconducting constrictions. Phys. Rev. B 27:6739, 1983.
[38] Cuevas JC, Martín-Rodero A, Levy-Yeyati A. Hamiltonian approach to the transport properties of superconducting quantum point contacts. Phys. Rev. B 54:7366, 1996.
[39] Cuevas JC, Martín-Rodero A, Levy-Leyati A. Microscopic origin of conducting channels in metallic atomic-size contacts. Phys. Rev. Lett. 80:1066, 1998.

[40] Crespo V, Maldonado A, Galvis JA, Kulkarni P, Guillamon I, Rodrigo JG, Suderow H, Vieira S, Banerjee S, Rodiere P. Scanning microscopies of superconductors at very low temperatures. Physica C 479:19, 2012.
[41] Rodrigo JG, Suderow H, Vieira S. On the use of STM superconducting tips at very low temperatures. Eur. Phys. J. B 40:483, 2004.
[42] Ambegaokar V, Baratoff A. Tunneling between superconductors. Phys. Rev. Lett. 10:486, 1963.
[43] Beenakker CWJ, van Houten H. Quantum transport in semiconductor nanostructures. Solid State Physics 44:1, 1991.
[44] Goffman MF, Cron R, Levy Yeyati A, Joyez P, Devoret MH, Esteve D, Urbina C. Supercurrent in atomic point contacts and Andreev states. Phys. Rev. Lett. 85:1590, 2000.
[45] Jäck B, Eltschka M, Assig M, Etzkorn M, Ast CR, Kern K. Critical Josephson current in the dynamical Coulomb blockade regime. Phys. Rev. B 93:020504(R), 2016.
[46] Hamidian MH, Edkins SD, Joo SH, Kostin A, Eisaki H, Uchida S, Lawler MJ, Kim E-A, Mackenzie AP, Fujita K, Lee J, Seamus Davis JC. Detection of a Cooper-pair density wave in $Bi_2Sr_2CaCu_2O_{8+x}$. Nature 532:343, 2016.
[47] da Silva Neto EH, Aynajian P, Baumbach RE, Bauer ED, Mydosh J, Ono S, Yazdani A. Detection of electronic nematicity using scanning tunneling microscopy. Phys. Rev. B 87:161117(R), 2013.
[48] Noat Y, Silva-Guillen JA, Cren T, Cherkez V, Brun C, Pons S, Debontridder F, Roditchev D, Sacks W, Cario L, Ordejon P, Garcia A, Canadell E. Quasiparticle spectra of 2H-$NbSe_2$: Two-band superconductivity and the role of tunneling selectivity. Phys Rev B 92:134510, 2015.
[49] Ruby M, Heinrich BJ, Pascual JI, Franke KJ. Experimental demonstration of a two-band superconducting state for lead using scanning tunneling spectroscopy. Phys. Rev. Lett. 114:157001, 2015.
[50] Hoffman JE, Hudson EW, Lang KM, Madhavan V, Uchida S, Davis JC. A four unit cell periodic pattern of quasi-particle states surrounding vortex cores in $Bi_2Sr_2CaCu_2O_{8+\delta}$. Science 295:466, 2002.
[51] Zhou BB, Misra S, da Silva Neto EH, Aynajian P, Baumbach RE, Thompson JD, Bauer ED. and Ali Yazdani. Visualizing nodal heavy fermion superconductivity in $CeCoIn_5$. Nat. Phys. 9:682, 2013.
[52] Caroli C, de Gennes PG, Matricon J. Bound fermion states on a vortex line in a type II superconductor. Phys. Lett. 9:307, 1964.
[53] Hess HF, Robinson RB, Waszczak JV. Vortex-core structure observed with a scanning tunneling microscope. Phys. Rev. Lett. 64:2711, 1990.
[54] Fente A, Herrera E, Guillamon I, Suderow H, Manas-Valero S, Galbiati M, Coronado E, Kogan VG. Field dependence of the vortex core size probed by STM. Phys. Rev. B 94:014517, 2016.
[55] Abrikosov AA. On the magnetic properties of superconductors of the second group. Sov. Phys. JETP 5:1174, 1957.
[56] Träuble H, Essman U. Flux-line arrangement in superconductors as revealed by direct observation. J. Appl. Phys. 39:4052, 1968.
[57] Pardo F, de la Cruz F, Gammel PL, Bucher E, Bishop DJ. Observation of smectic and moving Bragg glass phases in flowing vortex lattices. Nature 396:348, 1998.
[58] Fasano Y, Menghini M. Magnetic-decoration imaging of structural transitions induced in vortex matter. Superc. Sci. Technol. 21:023001, 2008.
[59] Tonomura A, Kasai H, Kamimura O, Matsuda T, Harada K, Shimoyama J, Kishio K, Kitazawa K. Motion of vortices in superconductors. Nature 397:308, 1999.
[60] Rubio-Bollinger G, Suderow H, Vieira S. Tunneling spectroscopy in small grains of superconducting MgB_2. Phys. Rev. Lett. 86:5582, 2001.

[61] Herrera E, Guillamon I, Galvis JA, Correa A, Fente A, Luccas RF, Mompean FJ, Garcia-Hernandez M, Vieira S, Brison JP, Suderow H. Magnetic field dependence of the density of states in the multiband superconductor β-Bi_2Pd. Phys. Rev. B 92:054507, 2015.
[62] Guillamon I, Suderow H, Vieira S, Cario L, Diener P, Rodiere P. Superconducting density of states and vortex cores of 2H-NbS_2. Phys. Rev. Lett. 101:166407, 2008.
[63] Gomes KK, Pasupathy AN, Pushp A, Ono S, Ando Y. and Ali Yazdani. Visualizing pair formation on the atomic scale in the high T_c superconductor $Bi_2Sr_2CaCu_2O_{8+}$. Nature 447:569–572, 2007.
[64] Levanyuk AP. Contribution to the theory of light scattering near the second-order phase-transition points. Sov. Phys. JETP 9:571, 1959.
[65] Ginzburg VL. Sov. Phys. Solid State 2:1284, 1960.
[66] Blatter G, Feigel'man MV, Geshkenbein VB, Larkin AI, Vinokur VM. Vortices in high temperature superconductors. Rev. Mod. Phys. 66:1125, 1994.
[67] Brandt EH. The flux-line lattice in superconductors. Rep. Prog. Phys. 58:1465, 1995.
[68] Larkin AI, Varlamov AA. Fluctuation phenomena in superconductors. Superconductivity, Bennemann and Ketterson, Springer, 2008.
[69] Guillamón I, Suderow H, Fernández-Pacheco A, Sesé J, Córdoba R, De Teresa JM, Ibarra MR, Vieira S. Direct observation of melting in a two-dimensional superconducting vortex lattice. Nat. Phys. 5:651–655, 2009.
[70] Berezinskii V. Destruction of long-range order in one-dimensional and two-dimensional systems possesing a continuous symmetry group. II. Quantum systems. Sov. Phys. JETP 34:610, 1972.
[71] Kosterlitz JM, Thouless DJ. Ordering, metastability and phase transitions in two-dimensional systems. J. Phys. C 6:1181, 1973.
[72] Halperin BI, Nelson DR. Theory of two-dimensional melting. Phys. Rev. Lett. 41:121, 1978.
[73] Young AP. Dislocation-mediated melting in two dimensions. Phys. Rev. B 19:2457, 1979.
[74] Zhuravlev V, Maniv T. Simple analytical model of vortex-lattice melting in two-dimensional superconductors. Phys. Rev. B 60:4277, 1999.
[75] Troyanovski AM, Aarts J, Kes PH. Collective and plastic vortex motion in superconductors at high flux densities. Nature 399:665, 1999.
[76] Guillamon I, Suderow H, Vieira S, Sese J, Cordoba R, De Teresa JM, Ibarra MR. Direct observation of stress accumulation and relaxation in small bundles of superconducting vortices in tungsten thin films. Phys. Rev. Lett. 106:077001, 2011.
[77] Olsen CJ, Reichhardt C, Nori F. Nonequilibrium dynamics phase diagram for vortex lattices. Phys. Rev. Lett. 81:3757–3760, 1998.
[78] Guillamón I, Córdoba R, Sesé J, De Teresa JM, Ibarra MR, Vieira S, Suderow H. Enhancement of long range correlations in a 2D vortex lattice by an incommensurate 1D disorder potential. Nat. Phys. 10:881–856, 2014.
[79] Moshchalkov V, Woerdenweber R, Lang W. Nanoscience and Engineering in Superconductivity. Springer-Verlag Berlin Heidelberg, Berlin, 2010.
[80] Daldini O, Martinoli P, Qlsen JL, Berner G. Vortex-line pinning by thickness modulation of superconducting films. Phys. Rev. Lett. 32:218, 1973.
[81] Hanaguri T, Kitagawa K, Matsubayashi K, Mazaki Y, Uwamoto Y, Takagi H. Scanning tunneling microscopy/spectroscopy of vortices in LiFeAs. Phys. Rev. B 85:214505, 2012.
[82] Iavarone M, Di Capua R, Karapetrov G, Koshelev AE, Rosenmann D, Claus H, Malliakas CD, Kanatzidis MG, Nishizaki T, Kobayashi N. Effect of magnetic impurities on the vortex lattice properties in $NbSe_2$ single crystals. Phys. Rev. B 78:174518, 2008.